ADVANCED FUNCTIONAL MATERIALS
www.afm-journal.de

Insight into the Interface Design for Li Metal Anode: Organic-Rich or Inorganic-Rich

Yijia Wang, Hongyu Hou, Karnpiwat Tantratian, Lyudmila V. Goncharova, Bolin Fu, Enzhong Jin, Parham Pirayesh, Hamid Abdolvand, Xin Pang, Lei Chen, Changhong Cao,* and Yang Zhao**

Microcracks and surface heterogeneity in solid-electrolyte interphase (SEI) induced by repeated plating/stripping of lithium (Li) metal exacerbate SEI fracture propagation and dendrite growth, which lead to unsatisfactory Coulombic efficiency and limited cycle life of Li metal anode. In this study, the hybrid artificial interfaces with controlled organic–inorganic ratios are designed and deep insight into their impacts on the electro-chemo-mechanical properties is obtained. The organic–inorganic ratios in the hybrid interfaces influence the mechanical properties, lithiophilicity, and diffusion kinetics of the interfaces, which in turn affect the nucleation, early growth, and repeated deposition/dissolution behavior of Li. It is found that increasing the inorganic ratio in the hybrid interface can realize significantly enhanced electrochemical performances. This work answers a key question for hybrid interfaces: should organic-rich or inorganic-rich be preferred in the hybrid interface? It is believed that this work will guide the future design of hybrid interfaces for Li metal anode and open up opportunities for the realization of next-generation Li metal batteries.

1. Introduction

Decarbonization of power generation and electrification of light-duty vehicles are critical measures to build climate resilience.[1] Conventional lithium-ion battery (LIB) that utilizes graphite anode is the dominant storage technology for electric vehicles and grid-scale storage.[2] The graphite anode with a theoretical capacity of 372 mAh g^{-1} and electrochemical redox potential of 0.1 V versus Li/Li^+, however, compromises the attainable energy density of the LIB. Replacing graphite anode with Li metal would enable a step change in the resulted energy density of the battery, due to the high theoretical gravimetric and volumetric capacity (3860 mAh g^{-1} and 2062 mAh cm^{-3}) and low electrochemical redox potential (−3.04 V vs standard hydrogen electrode) of Li metal.[3] Nevertheless, Li metal still suffers from inhomogeneous dendrite formation, unstable solid-electrolyte interphase (SEI), and dramatic volume change during the electrochemical process, which in turn deteriorates the Coulombic efficiency (CE) and cycling life of the battery. In this regard, much research efforts have been devoted to interfacial engineering, due to its tunability of a variety range of properties that affect Li deposition behavior and effectiveness in electrochemical performance enhancement.[4,5] An ideal artificial SEI should possess the following properties: 1) chemical and electrochemical stability, 2) mechanical stability with desirable elastic and plastic behavior; 3) superior lithiophilicity to lower Li nucleation overpotential and homogenize nucleation distribution, 4) fast Li-ion diffusion

Y. Wang, B. Fu, E. Jin, P. Pirayesh, H. Abdolvand, Y. Zhao
Department of Mechanical and Materials Engineering
University of Western Ontario
London, Ontario N6A 5B9, Canada
E-mail: yzhao628@uwo.ca

H. Hou, C. Cao
Department of Mechanical Engineering
McGill University
Montreal, Quebec H3A 0C3, Canada
E-mail: changhong.cao@mcgill.ca

K. Tantratian, L. Chen
Department of Mechanical Engineering
University of Michigan—Dearborn
Dearborn, MI 48128, USA
E-mail: leichn@umich.edu

L. V. Goncharova
Department of Physics and Astronomy
University of Western Ontario
London, Ontario N6A 3K7, Canada

X. Pang
CanmetMATERIALS
Natural Resources Canada
183 Longwood Road South, Hamilton, Ontario L8P0A5, Canada

The ORCID identification number(s) for the author(s) of this article can be found under https://doi.org/10.1002/adfm.202406426

DOI: 10.1002/adfm.202406426

kinetics, and 5) structural and compositional homogeneity to enable uniform ion flux.

Essentially, artificial SEIs should be chemically and electrochemically stable with good electron insulation, which has been widely studied and identified. The importance of the mechanical properties of SEI has also been gradually recognized in recent years. An optimum SEI should possess a desirable modulus to plasticize the protrusion of Li and enable smooth deposition.[6–8] It was suggested that the moderate elastic modulus of the SEI could increase the failure time and extremely high mechanical strength is pointless.[9] In addition, artificial SEI needs to display sufficient toughness to accommodate the large degree of plastic deformations, while remaining adherent.[10,11] The good flexibility and high toughness could also limit Li dendrite growth and penetration. However, the role of the plastic behavior of SEI has not been deeply understood. The experimental studies on tuning the mechanical properties of artificial SEI and their potential influences on the nucleation/growth of Li and electrochemical performance are very limited. In addition to the electro-chemo-mechanical stability, other factors such as lithiophilicity and interfacial kinetics, also play critical roles in the Li nucleation and growth behavior. Several Li nucleation and early growth models have been developed to elucidate the impacts of different factors that thermodynamically and kinetically affect Li deposition. As depicted in the heterogenous model, the energy barrier for nucleation is largely influenced by the wetting nature of the surfaces, and a lithiophilic surface facilitates the nucleus to reach a stable growth regime.[12] Besides the nucleation process, modulating subsequent growth and repeated Li deposition/dissolution behavior are also vital to elongating the lifespan of the Li metal anode. Based on the space charge model, the depletion of Li ions at the surface of the electrode under high-rate deposition induces the formation of a large space charge, which leads to the formation of ramified Li deposition.[13] In this case, the diffusion kinetics of the SEI significantly affect the Li deposition morphology. An SEI with higher diffusion kinetics could induce a higher Li-ion concentration beneath the SEI, which leads to spherical Li electrodeposits; In contrast, dendritic Li electrodeposits tend to form at the tip of the initial deposits when SEI possesses slow Li diffusion kinetics.[14] The artificial SEI with improved lithiophilicity, reduced nucleation barrier, and enhanced Li-ion charge transfer kinetics can realize uniform Li deposition and reduced dendrite formation. Very few artificial SEI fabrication strategies could realize the abovementioned properties concurrently. Consequently, the impacts of these electro-chemo-mechanical driving forces on the nucleation/growth behavior of Li and the resulting electrochemical performance are infrequently discussed.

Hybrid interfaces, such as dual-layers, organic–inorganic alloys, and laminated structures, were developed as effective approaches for controlling the compositions and properties of the artificial SEI for Li metal anodes, resulting in significantly improved electrochemical performances.[15,16] Among them, an organic–inorganic dual-layer structure inspired by the naturally-formed SEI could inherit the respective advantages from both organic and inorganic compounds.[17] It has been proven that hybrid interfaces containing both inorganic and organic layers provide the combined merits of high modulus and toughness.[18] In addition, the hybrid interfaces with anchored lithiophilic nucleation sites, including alloy seeds that exhibit a definite solubility in Li;[19] metal oxides (Al_2O_3,[20] ZnO,[21] TiO_2,[22] etc.) and organic materials[23,24] that can effectively lower the voltage hysteresis during repeated plating/stripping process. However, many questions remain unclear. For example, the fabrication of the hybrid interfaces with controllable organic–inorganic ratios has not been explored. Moreover, the potential effects of organic–inorganic ratios of the interface on resulted mechanical properties, diffusion kinetics and dendrite formation are rarely studied. Particularly, a key question needs to be answered: whether an organic-rich or an inorganic-rich interface is more favorable for Li metal anodes.

Herein, we first demonstrate the controllable fabrication of the hybrid artificial SEI for Li metal anode with different organic–inorganic ratios. Three typical compositions were realized: organic-rich interface, organic–inorganic-balanced interface, and inorganic-rich interface. The different organic–inorganic ratios of the hybrid interfaces result in the tuning of the mechanical properties, lithiophilicity, diffusion kinetics, and Li dendrite formation of the Li metal anode. The inorganic-rich interface possesses desirable flexibility to accommodate the stress induced by repeated Li deposition/dissolution process and high mechanical stiffness to regulate the uniform Li stripping/deposition and suppress the growth of Li dendrites. In addition, the inorganic-rich interface can realize the superior lithiophilicity and the fastest diffusion kinetics, which thereby influences the nucleation, early growth behavior, and final bulk deposition morphology of Li. The inorganic-rich interface enabled dendrite-free Li metal anodes with stable, long lifespan (> 3000 h), and low voltage hysteresis (≈150 mV at 3000 h) at 3 mA cm^{-2}, 1 mAh cm^{-2}, which outperforms its inorganic/organic-only counterparts and remarkably enhances the cycling performance of Li metal anode. The exceptional electrochemical performance was attributed to the synergistic effect of mechanical toughness, lithiophilicity, and diffusion kinetics of the designed artificial SEI.

2. Results and Discussion

In this research, artificial SEIs with desirable mechanical stiffness and flexibility, tunable lithiophilicity, and fast diffusion kinetics were designed to realize dendrite-free LMBs (**Figure 1a**). To ensure the mechanical robustness and flexibility of the artificial SEIs, a hybrid artificial SEI structure with tuned inorganic-organic ratios was engineered. The artificial SEIs employed alucone as an outer organic layer, due to its flexibility and capability of enabling dendrite-free deposition;[25] and TiO_2 as an inner inorganic layer, which exhibits faster diffusion kinetics compared with the widely explored Al_2O_3 and could effectively suppress dendrite growth.[26] Herein, we fabricated three artificial SEIs of an identical theoretical thickness (10 nm) on Li metal foils, with their lithiophilicity tuned by adjusting the thickness ratio between organic compounds (alucone) and inorganic compounds (TiO_2):[25,27] from L1, L2, to L3, the TiO_2 content inside the artificial interface increases, while the alucone content decreases. The L1, L2, to L3 are defined as organic-rich interfaces, organic–inorganic-balanced interfaces, and inorganic-rich interfaces, respectively. The structures of the artificial SEIs were characterized using time-of-flight secondary ion mass spectroscopy (ToF-SIMS), and a typical depth profile is presented in Figure 1b. Negatively charged fragments including AlC_2^- and

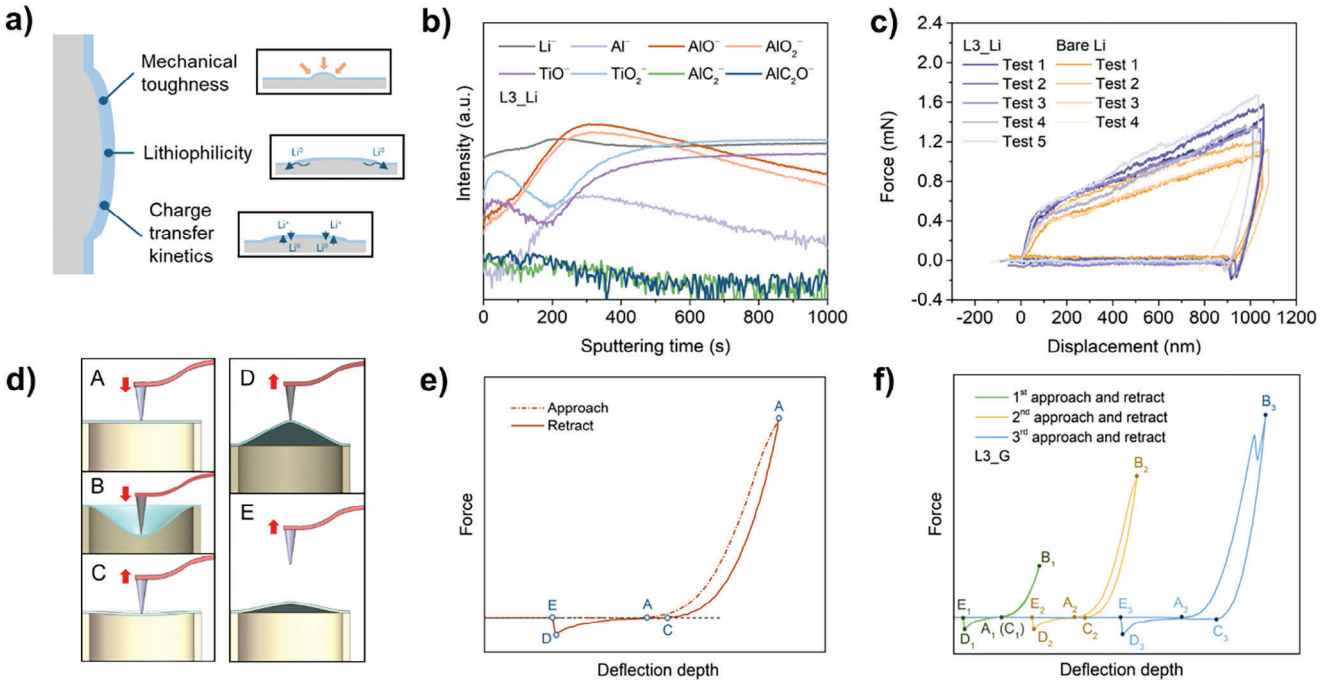

Figure 1. a) Properties of an ideal artificial SEI. b) The ToF-SIMS depth profile of L3_Li. c) Force-displacement curve from the Berkovich nanoindentation test. d) Schematic showing five key stages during the deflection tests under large loads, labeled with A-E (point A, effective load ramp-up starts; point B, at maximum deflection depth; point C, when the applied load was diminished and pull-off starts; point D, right before tip-sample separation; point E, when tip-sample was just separated and the tip was resistance free). e) Representative loading–unloading curve from AFM deflection experiment marked with corresponding stages illustrated in d). f) Representative loading–unloading curves from the AFM deflection experiment of sample L3_G tested with different maximum applied loads.

AlC_2O^- were attributed to the presence of alucone, while TiO^- and TiO_2^- signals were used to investigate the TiO_2 layer. The intensity of AlC_2^- and AlC_2O^- increases before the rise of TiO^- and TiO_2^- signals, confirming the outer organic alucone layer and inner inorganic TiO_2 structure of the artificial SEIs. For L3_Li (Figure 1b), the AlC_2^- and AlC_2O^- signals reached the highest intensity after ≈195 s of sputtering and the TiO^- and TiO_2^- signals were maximized at ≈550 s. The depth profiles of L1_Li and L2_Li were provided in the Supporting Information. For L1_Li, the AlC_2^- and AlC_2O^- signals reached the maximum intensity after ≈350 s, while the TiO^- and TiO_2^- signals peaked at ≈530 s (Figure S1, Supporting Information, left). The L2_Li (Figure S1, Supporting Information right) contained a thinner alucone layer and a thicker TiO_2 layer relative to L1_Li, in which the AlC_2^- and AlC_2O^- signals achieved the highest point after ≈285 s of sputtering and the TiO^- and TiO_2^- signals reached a plateau after ≈500 s. It is important to note that ToF-SIMS only provides semiquantitative results due to the matrix effects.[28] The composition and structure of the artificial SEI were further examined using Rutherford backscattering spectroscopy (RBS). As presented in Figure S2 (Supporting Information), all spectra demonstrated a distinct dual-layered structure with the Al signal present in the top layer and the Ti signal present in the bottom layer adjacent to the Li substrate. From L1_Li to L3_Li, the thickness of the alucone layer decreases and the thickness of the TiO_2 layer increases, indicating the successful fabrication of artificial SEI using ALD and MLD with the controlled organic–inorganic ratios including organic-rich interfaces, organic–inorganic-balanced interfaces, and inorganic-rich interfaces.

The mechanical properties of the different hybrid interfaces were studied by the Berkovich nanoindentation test and atomic force microscopy (AFM) deflection tests. The elastic modulus of artificial SEI L3 coated Li (L3_Li) and bare Li were compared. From the Berkovich nanoindentation test, the average elastic modulus obtained on L3_Li is 68% higher than that on bare Li (Figure 1c; Figure S3, Supporting Information), indicating the artificial SEI would mitigate dendrite growth and promote uniform electrodeposition. The nanoindentation processes of bare Li and L3_Li were recorded and included in the Supplemental Video files. AFM deflection tests on suspended artificial SEIs were performed to investigate their mechanical properties, where SEIs were deposited on perforated (2.5 μm in diameter) transmission electron microscopy (TEM) grids covered with monolayer graphene, denoted as L1_G, L2_G, and L3_G, respectively. First, low-load (≤100 nN) elastic deflection tests were carried out at over ten different locations of each sample. Elastic moduli were calculated by fitting the obtained force-displacement curves into a classic mechanics model (see Supplementary Experimental S2, Supporting Information). The results revealed that the 2D elastic moduli of the three SEI cases are very close in range (1091 ± 61 N m^{-1} of L3_G, 1136 ± 49 N m^{-1} of L2_G, 973 ± 52 N m^{-1} of L1_G), suggesting that they possess comparable deformation resistance in the elastic regime (Figure S4, Supporting Information).

Subsequent to the initial elastic deflection tests, a series of deflection experiments at higher loads were conducted to assess the resilience of the SEI films under larger deformations. Progressive plastic deformations were observed in all three types of SEI samples mentioned above, as the experimentally-set maximum deflection force (F_{max}) was incrementally increased but no catastrophic fracture was achieved on any of the samples within the instrumentation force capacity. A schematic illustrating five key stages (marked with A-E) during the deflection tests at high loads (Figure 1d) and a corresponding representative loading–unloading curve are presented in Figure 1e. The five key stages include: point A, when effective load ramp-up starts; point B, at maximum deflection depth; point C, when the applied load was diminished and the pull-off starts; point D, right before tip-sample separation; point E, when tip-sample was just separated and the tip was resistance free. The hysteresis between the loading and unloading curves is an indication of energy dissipation and the sudden small load drop in the third loading cycle, B3 (Figure 1f) is a manifestation of slippage during the deflection tests when large loads are applied, commonly seen in this type of experiment.[29] It can be seen from Figure 1e that A and C did not overlap but have a gap distance in between (L_{AC} (Z_C-Z_A)), which represents the amount of plastic deformation of the film and was found to be in a proportional relationship with the maximum set load F_{max} (Figure 1f). For instance, in the case of sample L3_G (Figure 1f), while no noticeable plastic deformation was observed when the film was deflected with a maximum load of 400 nN in the first loading cycle ($L_{A_1C_1} = 0$), the apparent gap distance between A and C can be seen when larger loads were applied in the subsequent cycles ($L_{A_3C_3} > L_{A_2C_2} > L_{A_1C_1}$). Such plastic deformations caused the SEI films to become elongated and saggier over the hole, and delayed the "pull-off" point as indicated by the distance between points C and D, L_{CD} (Z_C- Z_D) which was found to increase with respect to the degree of plastic deformations. When an elongation/max force ratio (L_{CD}/F_{max}) is employed to evaluate the plastic resistance to indentation load, it is shown in Figure S5 (Supporting Information) that L3_G films exhibited the highest ratio among the three types of films. This observation suggests a propensity for augmented plastic deformation in L3_G films. Consequently, during the deposition and stripping of Li, the L3_G films exhibit increased deformation, leading to a larger surface area, which offers greater potential for homogenizing the ion flux. In addition, AFM tapping mode imaging of the SEI films before and after each deflection tests were performed and it was shown in the images that the films were elongated and became saggier with larger loads (Figure S6, Supporting Information). It should be noted that pure graphene would not exhibit obvious plastic deformation as identified here[30] and the organic nature of the SEI films is believed to be responsible for such behaviors. Similar plastic behaviors were also shown in samples of L1_G and L2_G films (Figure S7, Supporting Information). From the understanding of the mechanical properties of different hybrid interfaces, it is found that tuning the organic–inorganic ratios in the hybrid interfaces has a small influence on the elastic modulus, however, the inorganic-rich interfaces (L3_Li) could accommodate higher plastic deformation compared to the organic-rich interfaces (L1_Li) and organic–inorganic-balanced interfaces (L2_Li), which

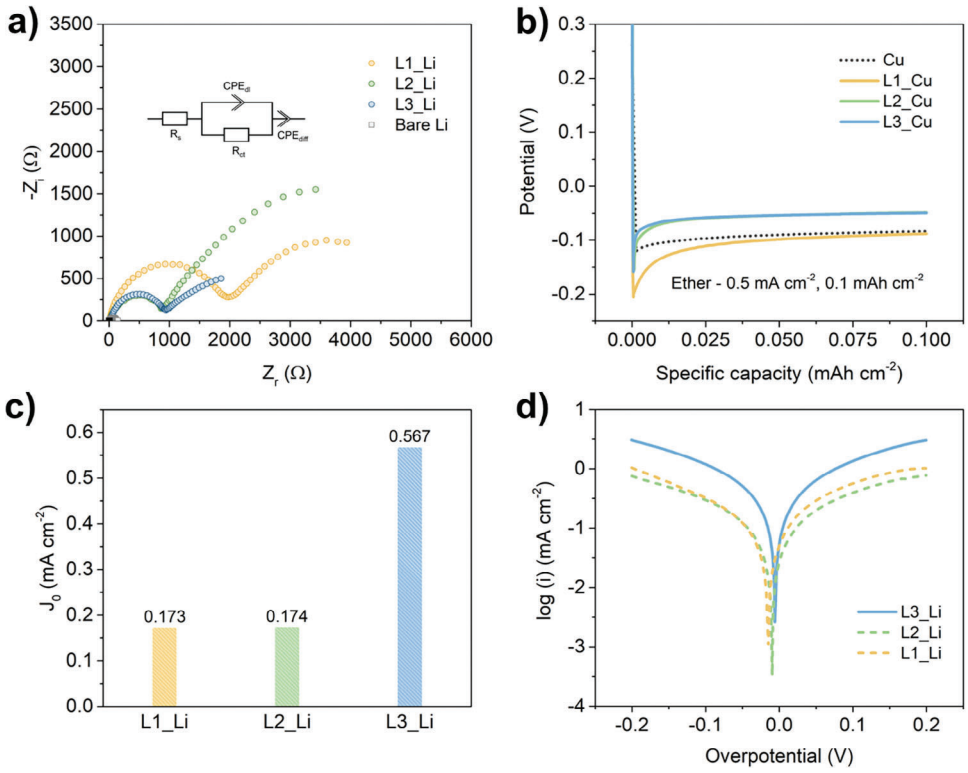

Figure 2. a) Nyquist plots of L1_Li, L2_Li, L3_Li, and bare Li before cycling. b) Nucleation overpotential on Cu, L1_Cu, L2_Cu, and L3_Cu. c) Tafel plots and d) corresponding exchange current density of L1_Li, L2_Li, and L3_Li.

could suppress the Li dendrite formation and penetration more effectively.

Electrochemical impedance spectroscopy (EIS) was employed to probe the impedance of the fabricated artificial SEIs. The Nyquist plots of L1_Li | L1_Li, L2_Li | L2_Li, L3_Li | L3_Li, and Li | Li are depicted in **Figure 2a**. In the high-frequency region, the intercept at the real axis refers to the bulk resistance from the liquid electrolyte, while the diameter of the semi-circle in the high-frequency region is related to the electrochemical charge transfer resistance (R_{ct}) of symmetric cells. The Li | Li symmetric cell presented the lowest R_{ct} value of 1.7 Ω, which was attributed to the spontaneously formed thin SEI upon contact with electrolyte.[31] The L1_Li | L1_Li, L2_Li | L2_Li, L3_Li | L3_Li symmetric cells exhibit much higher R_{ct} values of 1861, 794, and 865 Ω, respectively. The much higher R_{ct} values of Li with artificial SEI are attributed to the poor electron and ion transfer kinetics of TiO_2 and alucone films before lithiation,[22,32] which prevents the electrons from reducing the electrolyte.[32] Detailed fitting parameters for the equivalent circuit modeling of L1_Li | L1_Li, L2_Li | L2_Li, L3_Li | L3_Li, and Li | Li symmetric cells are included in Table S1 (Supporting Information).

To investigate the initial nucleation and early-stage growth of Li on the three artificial SEIs, artificial SEIs L1, L2, and L3 were fabricated on copper (Cu) foils, respectively, denoted as L1_Cu, L2_Cu, and L3_Cu. Two critical characteristic overpotentials were evaluated: nucleation overpotential and growth overpotential. Nucleation overpotential is determined by the initial "dip" of the voltage profile during the plating process,[19] which represents the heterogeneous nucleation barrier resulting from a combination of charge transfer process and interfacial formation; while mass transfer of Li ions from bulk electrolyte through the developed interface and formation of subsequent Li nuclei give rise to growth overpotential.[4,33] In Figure 2b, the Li nucleation and growth overpotential were investigated on L1_Cu, L2_Cu, L3_Cu, and bare Cu. Under a current density of 0.5 mA cm^{-2}, the initial nucleation overpotential for L1_Cu, L2_Cu, L3_Cu, and bare Cu are −0.20, −0.16, −0.16, and −0.12 V, respectively. The slightly higher nucleation overpotentials observed on Cu coated with the artificial SEI compared with that on bare Cu are induced by the charge transfer at the artificial SEI.[34] The Li growth overpotentials on L1_Cu, L2_Cu, L3_Cu, and bare Cu were determined at capacity of 0.1 mAh cm^{-2}, which were −0.09, −0.05, −0.05, and −0.08 V, respectively, indicating that L2 and L3 artificial SEIs facilitated the early-stage growth of electrodeposited Li.

The interfacial kinetics of the artificial SEIs on Li metal anodes were examined through Tafel analysis.[14,35] In Figure 2c, the Tafel plots derived from cyclic voltammetry of the corresponding Li symmetric cells were presented. The exchange current densities that reflect the charge transfer kinetics of L1, L2, and L3 were determined from the Tafel plots. As shown in Figure 2d, the exchange current density for L1, L2, and L3 are 0.173, 0.174, and 0.567 mA cm^{-2}, respectively, demonstrating the faster interfacial kinetics of L3 (inorganic-rich interfaces).

The nucleation and growth behavior of deposited Li metal on modified Cu current collectors was investigated to evaluate the dendrite suppression capability of the artificial SEI. To investigate the evolution of Li nuclei during electrodeposition, Li was deposited galvanostatically at 0.5 mA cm^{-2} on corresponding Cu foils and the surface morphology of the deposited Li on Cu, L1_Cu, L2_Cu, and L3_Cu foils after fixed amount of Li deposition (0.1, 0.5, and 1 mAh cm^{-2}) was characterized by ex situ SEM. As shown in **Figure 3a**, deposited Li on bare Cu foil in ether-based electrolyte exhibits typical circular morphology, which corresponds well with the previous report.[4] The particle size of the Li deposits on bare Cu increases with the increase in deposition capacity. At 1 mAh cm^{-2}, Li deposits with rough surfaces were observed. In contrast, Li deposits demonstrate different nucleation and growth behavior on modified Cu current collectors. On L1_Cu foil, mossy Li nucleation was observed at a low deposition capacity of 0.1 mAh cm^{-2}. These nuclei continue to merge and form large particles with small nuclei present on the surface. On L2_Cu and L3_Cu foils, Li nucleated and formed bowl-like structures at the initial stage of growth. At 0.5 mAh cm^{-2}, deposition of Li nuclei on the concave surface of the established bowl-like structure and fusing of small Li nuclei were observed. With further increase in deposition capacity (1 mAh cm^{-2}), enclosed Li particles emerged. Differing from the moderately roughened surface of the Li particles that appeared on L2_Cu foil, the surface of the Li particles formed on L3_Cu foil is smooth. Based on the experimental findings, a Li deposition mechanism on the surface of different extents of lithiophilicity was proposed and illustrated in Figure 3b. At the beginning of nucleation, more nuclei are preferentially formed on the substrate surface with a higher degree of lithiophilicity, due to the lower nucleation barrier. The sparse initial Li nucleation ultimately leads to dendritic Li deposition, as observed on the L1_Cu. In the subsequent growing process, bowl-like Li deposits started to form on top of the initial nucleates. On L2_Cu, larger bowl-shaped deposits are likely induced by the less dense Li nucleation, while the initial dense Li nucleation gives rise to uniform, smaller-sized bowl-shaped deposits on L3_Cu (inorganic-rich interfaces) and enables uniform Li plating. The nucleation and growth behavior were also captured at lower magnification to demonstrate that the trend observed is not restricted to localized areas (Figure S8, Supporting Information). Such nucleation and initial growth behavior account for the outstanding electrochemical performance of Li metal anodes with L3 artificial SEI.

Hypothesizing based on the experimental findings, variations in Li morphologies across different surfaces may be attributed to different levels of lithiophilicity. With a substantial volume fraction of lithiophilic TiO_2, L3_Cu demonstrates the lowest Li nucleation barrier among other surfaces. This results in achieving the smallest contact angle and dense Li nuclei formation on the surface, facilitating the compact growth of the deposited Li layer. In contrast, L1_Cu, with a poor lithiophilic surface, exhibits larger contact angles and sparse Li nucleation sites, which unfortunately promote the formation of Li dendrites. The phase-field modeling, as depicted in Figure 3c, further supports the influence of Li nuclei shape and density on the surface in regulating the final Li morphologies.

The electrochemical performance of the artificial SEI was evaluated in symmetrical, anode-free, and full-cell configurations in ether-based electrolyte (1 M lithiumbis(trifluoromethanesulfonyl)imide (LiTFSI) in 1,3-dioxolane (DOL)/1,2-dimethoxyethan (DME) (1:1 w/w) with 2 wt.% lithium nitrate ($LiNO_3$) additive). At a current density of 3 mA cm^{-2} and a capacity of 1 mAh cm^{-2}, Li_L3 | L3_Li symmetric cell exhibited

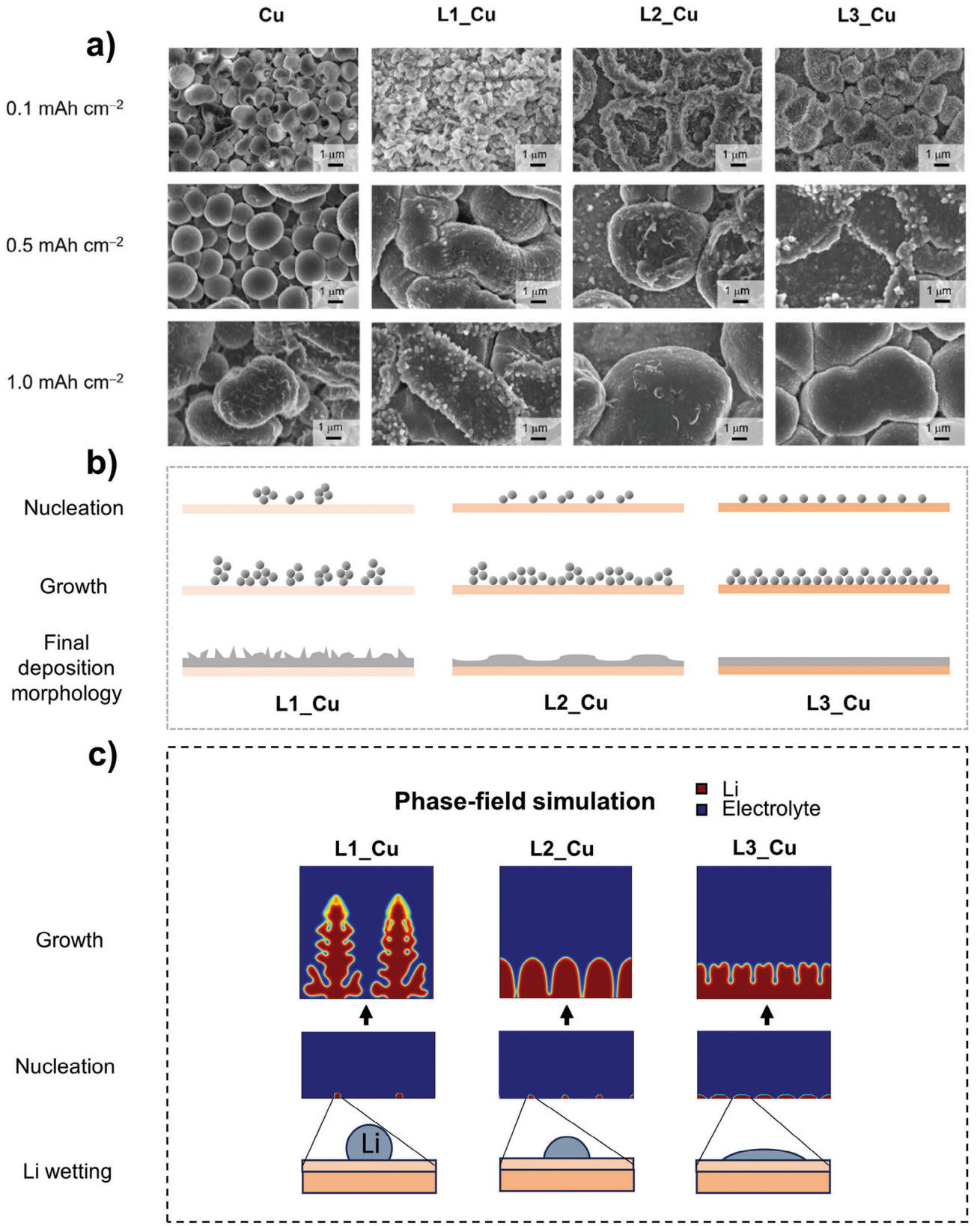

Figure 3. a) The SEM images of Li metal deposition at different capacities (0.1, 0.5, and 1 mAh cm^{-2}) under a deposition current density of 0.5 mA cm^{-2} on bare and modified Cu substrates. b) Proposed Li metal deposition mechanism. c) Phase-field simulation results revealing distinct Li morphologies influenced by varied nuclei shapes and distribution, highlighting the influences of different Li wettability on the L1_Cu, L2_Cu, and L3_Cu surfaces.

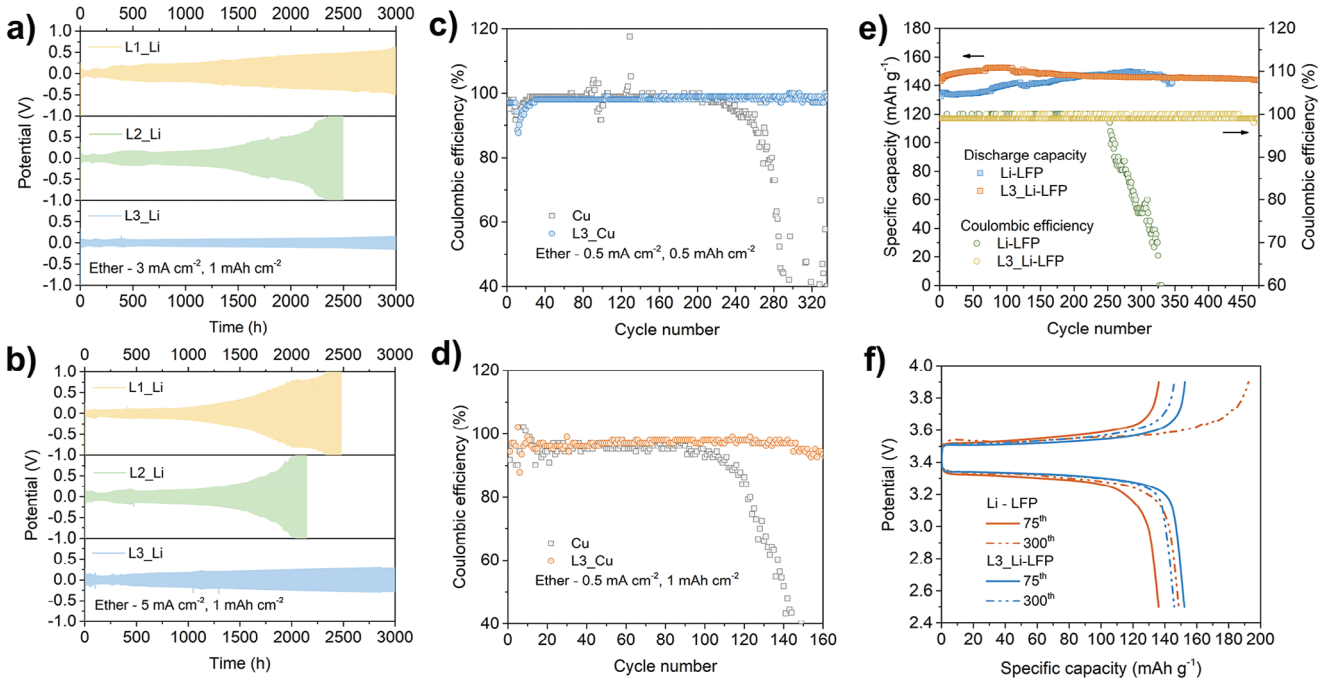

Figure 4. Electrochemical performance of symmetric cells L1_Li | L1_Li, L2_Li | L2_Li, and L3_Li | L3_Li under a) 3 mA cm^{-2}, 1 mAh cm^{-2} and b) 5 mA cm^{-2}, 1 mAh cm^{-2}. Coulombic efficiency of Li | Cu and Li | L3_Cu cells under c) 0.5 mA cm^{-2}, 0.5 mAh cm^{-2} and d) 0.5 mA cm^{-2}, 1 mAh cm^{-2}. e) Galvanostatic long term cycling performance of Li | LFP and L3_Li | LFP at 1 C. f) Voltage profiles of Li | LFP and L3_Li | LFP at 75th and 300th cycle.

stable cycling for above 3000 h, with limited stripping/plating overpotential increase during cycling (≈100 mV before 2000 h and gradually increases to ≈150 mV at 3000 h), as shown in **Figure** 4a. In contrast, Li_L1 and Li_L2 showed a much more pronounced hysteresis augmentation, which exceeded 0.5 V after ≈2500 and ≈1800 h, respectively. At an increased current density of 5 mA cm^{-2}, Li_L3 | L3_Li symmetric cell lasted for 3000 h, with final stripping/plating overpotential of ≈270 mV, while the voltage hysteresis of Li_L1 and Li_L2 exceeded 1 V after ≈2300 h and ≈2000 h, respectively (Figure 4b). The Li_L3 | L3_Li symmetric cell was also evaluated at a current density of 3 mA cm^{-2} and a capacity of 3 mAh cm^{-2}, and demonstrated stable cycling for over 3000 h with stable stripping/plating overpotential (Figure S9, Supporting Information). The thickness of the constructed artificial SEI L3 was also identified to be optimal, which outperforms the SEIs of similar composition with halved (0.5L3) or doubled total thickness (2L3) in terms of galvanostatic cycling performance, under a moderate current density of 3 mA cm^{-2} (Figure S10, Supporting Information (left)) and a high current density of 5 mA cm^{-2} (Figure S10, Supporting Information (right)). Compared with bare Li metal anodes, L3_Li demonstrated an elongated cycle life and lower stripping/plating overpotential during cycling (Figure S11, Supporting Information). Other than the ether-based electrolyte, the electrochemical performance of L1_Li, L2_Li, and L3_Li was also evaluated in the carbonate-based electrolyte (1 M $LiPF_6$ in ethylene carbonate (EC): diethyl carbonate (DEC): dimethyl carbonate (DMC) (1:1:1 v/v/v)). Similar to the performance observed in ether-based electrolytes, L3_Li exhibited the best long-term cycling performance among the three compositions (Figure S12, Supporting Information (left)) as well as L3 of different thicknesses (Figure S12, Supporting Information (right)). Compared with that in carbonate-based electrolytes, the significantly enhanced electrochemical performance observed in ether-based electrolytes was attributed to the elastomeric oligomers formed on the electrodes due to the presence of DOL,[36] which functions synergistically with the artificial SEI. The interfacial impedance of artificial SEIs developed in both ether-based electrolyte and carbonate-based electrolyte were evaluated. As shown in Figure S13 (Supporting Information), the interfacial impedance of the artificial SEI after cycling for 100 cycles in the ether-based electrolyte is significantly higher than that in the carbonate-based electrolyte, which corresponds well to the electrochemical performance observed in the two electrolyte systems.

The electrochemical performance of dual-layered L3 was also compared with that of the individual alucone and TiO_2 layers. In Figure S14 (Supporting Information), the long-term cycling performance of the Li metal with individual alucone (Alu_Li) and TiO_2 (TiO_2_Li) layers was presented. Under a current density of 3 mA cm^{-2} and a capacity of 1 mAh cm^{-2}, the overpotential of Alu_Li and TiO_2_Li exceeded 1 V after ≈1800 and ≈900 h, respectively. At an increased current density of 5 mA cm^{-2}, Alu_Li and TiO_2_Li lasted for ≈670 and ≈730 h, before the overpotential reached 1 V. The results demonstrated the advantages of organic–inorganic hybrid artificial SEI design fabricated by ALD and MLD techniques, which agrees well with our previous study.[37] The inverse L3 composed of 70 cycles of outer ALD TiO_2 layer and 6 cycles of inner MLD alucone layer were also fabricated on Li metal. In Figure S15 (Supporting Information), the inverse L3_Li exhibited notably higher overpotential compared with that of L3_Li, when cycled under 3 mA cm^{-2}, 1 mAh cm^{-2}

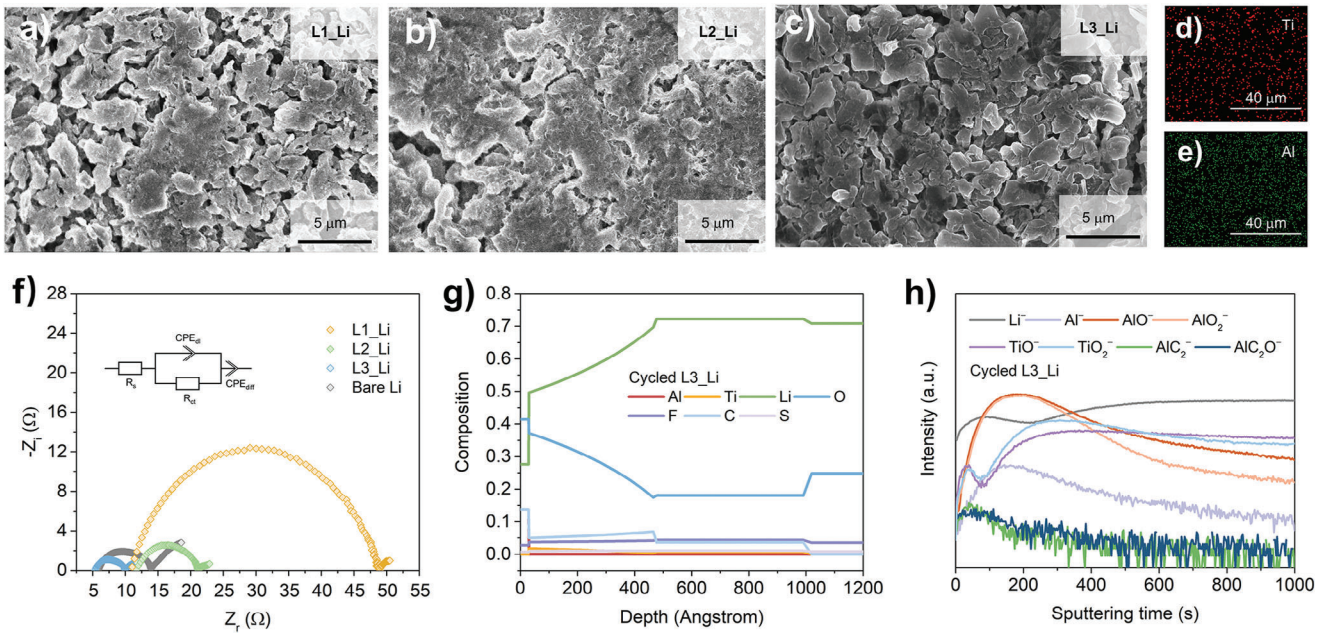

Figure 5. The top-view SEM images of a) L1_Li, b) L2_Li, and c) L3_Li after 100 cycles. The EDX elemental mapping of d) Ti, and e) Al for L3_Li after 100 cycles. f) Nyquist plots of L1_Li, L2_Li, L3_Li, and Li after 250 cycles. g) The calculated RBS depth profile of cycled L3_Li. h) The ToF-SIMS depth profile of cycled L3_Li.

and 5 mA cm^{-2}, 1 mAh cm^{-2}, suggesting the inner inorganic outer organic structure of L3_Li presents enhanced stability over cycling.

The artificial SEI L3 was then fabricated on Cu foil, and a Li | Cu anode-free configuration was employed to evaluate the Li stripping/plating efficiency on L3-modified Cu current collectors. As shown in Figure 4c, L3_Cu enabled an average Li plating/stripping CE of above 98.1% for 300 cycles under 0.5 mA cm^{-2}, 0.5 mAh cm^{-2}, while bare Cu only displayed an average CE of 93.6%. By increasing the plating capacity to 1 mAh cm^{-2}, an average CE of 97.1% for the first 150 plating/stripping cycles was achieved on L3_Cu, whereas an average CE of 88.1% was observed on bare Cu current collectors (Figure 4d). The results correspond well with the nucleation and growth behavior in Figures 2b and 3a, in which the lithiophilic L3 SEI enabled dense Li deposition and mitigated dead Li formation during cycling, therefore enhancing the plating/stripping CE.

The L3_Li was also paired with the $LiFePO_4$ (LFP) cathode and evaluated in the ether-based electrolyte. The L3_Li | LFP full cell delivered a high initial specific capacity of 143 mAh g^{-1}, with a high CE of above 99% for 475 cycles (Figure 4e). At 75th and 300th cycle, the L3_Li | LFP full cell delivered specific capacities of 152 and 146 mAh g^{-1}, respectively (Figure 4f). In contrast, Li | LFP full cell only exhibited an initial specific capacity of 133 mAh g^{-1} and lower specific capacities during cycling (Figure 4e), due to the larger charge/discharge voltage gap induced by higher Li plating/stripping overpotential on bare Li, as observed in Figure 4f. The CE of Li | LFP maintained above 99% for the first 250 cycles then decayed drastically afterward (Figure 4e).

Through tailoring the composition of the artificial SEI, the morphology of the Li deposition can be tuned, which leads to different plating/stripping behavior across cycling. In this study, the top surface of L1_Li, L2_Li, and L3_Li after 100 cycles were investigated using SEM. As shown in **Figure** 5a, porous Li deposition was observed on the L1_Li surface. Coalescence of Li deposits accompanied by minor mossy Li growth was found on L2_Li (Figure 5b) while Li deposits fusion with a smooth surface was seen on L3_Li (Figure 5c). The surface of bare Li after 100 cycles was also included in Figure S16 (Supporting Information), in which large porous Li deposits were shown. The morphology observed on L1_Li, L2_Li, L3_Li, and bare Li agrees well with the electrochemical performance presented in the previous section, in which L3_Li | L3_Li symmetric cells delivered the longest cycle life with the lowest voltage hysteresis among the three artificial SEIs. The surface of the L3_Li was further investigated using energy-dispersive X-ray (EDX) spectroscopy. From the EDX spectrum presented in Figure 5d,e, Ti and Al are uniformly distributed on the L3_Li electrode surface, indicating that the artificial SEI persisted on the surface of Li and ensured stable Li stripping/plating during long-term cycling. The impedances of cycled L1_Li | L1_Li, L2_Li | L2_Li, L3_Li | L3_Li, and Li | Li symmetric cells were assessed using EIS (Figure 5f). After cycling at a current density of 5 mA cm^{-2} and a capacity of 1 mAh cm^{-2} for 250 cycles, the lithiated artificial SEI showed higher ionic conductivity compared with the pristine state, and the R_{ct} of L1_Li | L1_Li, L2_Li | L2_Li, and L3_Li | L3_Li drastically decreased to 36.2, 8.2, and 4.5 Ω, respectively. The Li | Li shows an increase in interfacial impedance with R_{ct} increased to 8.167 Ω after 250 cycles. The higher R_{ct} values of L1_Li, L2_Li, and bare Li imply slower charge transfer kinetics of the developed SEIs, which leads to a non-uniform Li plating/stripping process (as observed in top-view SEM images of the surface morphology of cycled Li with artificial SEI in Figure 5a,b) and increase in polarization across long-term cycling. Detailed fitting parameters for the equivalent

circuit modeling of L1_Li | L1_Li, L2_Li | L2_Li, L3_Li | L3_Li, and Li | Li symmetric cells after 250 cycles are included in Table S2 (Supporting Information). The interfacial impedance of L3_Li was evaluated along cycles to understand the microstructure evolution of the artificial SEI. In Figure S17 (Supporting Information), the interfacial impedance of L3_Li gradually decreases over cycles, which facilitates the transport of Li ions during cycling. The interfacial impedance of L3 after 200 cycles demonstrates no observable change compared with that at 250 cycles (Table S3, Supporting Information), showing the stability of the artificial SEI. The RBS and ToF-SIMS depth profiles of the cycled L3_Li are shown in Figure 5g,h, respectively. From the RBS and ToF-SIMS depth profiles, we can see that the dual-layered structure remained after cycling with Ti penetrated to the deeper level of the Li metal anode. The presence of F and S signals is mainly attributed to the decomposition of the electrolyte salt during the cycling process.

3. Conclusion

In this work, the influence of the organic–inorganic ratio was first understood in the hybrid interfaces on the electro-chemo-mechanical properties. Three types of interfaces were fabricated: organic-rich interface, organic–inorganic-balanced interface, and inorganic-rich interface. It is found that the organic–inorganic ratio can affect the mechanical properties, lithiophilicity, and charge transfer kinetics in the hybrid interfaces, resulting in the controlling of the Li electrodeposition morphology and electrochemical performances. First, increasing the inorganic ratio in the interface could accommodate higher plastic deformation, which could effectively suppress the growth of Li dendrites. Secondly, the inorganic-rich interface exhibits the lowest Li nucleation and growth overpotential and highest exchange current density, indicating its optimal lithiophilicity and charge transfer kinetics. Thirdly, the morphology of Li electrodeposits during the early stage of plating on artificial SEI-modified Cu was investigated by SEM. Different from the growth behavior observed on the inorganic-rich interface (L1_Cu) and organic–inorganic-balanced interface (L2_Cu), the coalescence of small Li nucleation forming large Li deposits with smooth surfaces was observed on the inorganic-rich interface (L3_Cu), suggesting the effectiveness of the inorganic-rich interface in inducing uniform Li deposition. In addition, the observation from the electrochemical performance is consistent with electro-chemo-mechanical properties. The inorganic-rich interface (L3) exhibits the most stable cycling performances in symmetrical, anode-free, and full-cell configurations. This work provides a new understanding of the design of the hybrid artificial interface for Li metal anode, especially the insight into the functions of inorganic and organic compounds in the hybrid interfaces. It will guide the future design of artificial interfaces for Li metal anode and open up opportunities for the realization of next-generation energy-dense battery systems based on Li metal chemistries.

Supporting Information

Supporting Information is available from the Wiley Online Library or from the author.

Acknowledgements

Y.W., H.H., and K.T. contributed equally to this work. This research was supported by the Natural Science and Engineering Research Council of Canada (NSERC), the Canada Foundation for Innovation (CFI), and the University of Western Ontario (UWO).

Conflict of Interest

The authors declare no conflict of interest.

Data Availability Statement

The data that support the findings of this study are available from the corresponding author upon reasonable request.

Keywords

dual-layer interface, electro-chemo-mechanical properties, hybrid artificial SEI, Li metal anode

Received: April 16, 2024
Revised: May 25, 2024
Published online: June 16, 2024

[1] S. J. Davis, N. S. Lewis, M. Shaner, S. Aggarwal, D. Arent, I. L. Azevedo, S. M. Benson, T. Bradley, J. Brouwer, Y.-M. Chiang, C. T. M. Clack, A. Cohen, S. Doig, J. Edmonds, P. Fennell, C. B. Field, B. Hannegan, B.-M. Hodge, M. I. Hoffert, E. Ingersoll, P. Jaramillo, K. S. Lackner, K. J. Mach, M. Mastrandrea, J. Ogden, P. F. Peterson, D. L. Sanchez, D. Sperling, J. Stagner, J. E. Trancik, et al., *Science* **2018**, *360*, eaas9793.
[2] P. Albertus, J. S. Manser, S. Litzelman, *Joule* **2020**, *4*, 21.
[3] D. Lin, Y. Liu, Y. Cui, *Nat. Nanotechnol.* **2017**, *12*, 194.
[4] A. Pei, G. Zheng, F. Shi, Y. Li, Y. Cui, *Nano Lett.* **2017**, *17*, 1132.
[5] X. R. Chen, B. C. Zhao, C. Yan, Q. Zhang, *Adv. Mater.* **2021**, *33*, 2004128.
[6] Y. Gao, B. Zhang, *Adv. Mater.* **2023**, *35*, 2205421.
[7] S. Li, X.-S. Wang, B. Han, C. Lai, P.-R. Shi, J.-B. Ma, S.-W. Wang, L.-H. Zhang, Q. Liu, Y.-H. Deng, Y.-B. He, Q.-H. Yang, *Small* **2022**, *18*, 2106427.
[8] R. Xu, X.-Q. Zhang, X.-B. Cheng, H.-J. Peng, C.-Z. Zhao, C. Yan, J.-Q. Huang, *Adv. Funct. Mater.* **2018**, *28*, 1705838.
[9] X. Shen, R. Zhang, X. Chen, X.-B. Cheng, X. Li, Q. Zhang, *Adv. Energy Mater.* **2020**, *10*, 1903645.
[10] W. Liu, P. Liu, D. Mitlin, *Adv. Energy Mater.* **2020**, *10*, 2002297.
[11] B. Li, Y. Chao, M. Li, Y. Xiao, R. Li, K. Yang, X. Cui, G. Xu, L. Li, C. Yang, Y. Yu, D. P. Wilkinson, J. Zhang, *Electrochem. Energy Rev.* **2023**, *6*, 7.
[12] D. R. Ely, R. E. García, *J. Electrochem. Soc.* **2013**, *160*, A662.
[13] J.-N. Chazalviel, *Phys. Rev. A* **1990**, *42*, 7355.
[14] X.-R. Chen, Y.-X. Yao, C. Yan, R. Zhang, X.-B. Cheng, Q. Zhang, *Angew. Chem., Int. Ed.* **2020**, *59*, 7743.
[15] T.-U. Wi, S. O. Park, S. J. Yeom, M.-H. Kim, I. Kristanto, H. Wang, S. K. Kwak, H.-W. Lee, *ACS Energy Lett.* **2023**, *8*, 2193.
[16] L. Fan, B. Sun, K. Yan, P. Xiong, X. Guo, Z. Guo, N. Zhang, Y. Feng, K. Sun, G. Wang, *Adv. Energy Mater.* **2021**, *11*, 2102242.
[17] X.-B. Cheng, C. Yan, X.-Q. Zhang, H. Liu, Q. Zhang, *ACS Energy Lett.* **2018**, *3*, 1564.
[18] P. Pirayesh, K. Tantratian, M. Amirmaleki, F. Yang, E. Jin, Y. Wang, L. V. Goncharova, J. Guo, T. Filleter, L. Chen, Y. Zhao, *Adv. Mater.* **2023**, *35*, 2301414.

[19] K. Yan, Z. Lu, H.-W. Lee, F. Xiong, P.-C. Hsu, Y. Li, J. Zhao, S. Chu, Y. Cui, *Nat. Energy* **2016**, *1*, 1.
[20] A. C. Kozen, C.-F. Lin, A. J. Pearse, M. A. Schroeder, X. Han, L. Hu, S.-B. Lee, G. W. Rubloff, M. Noked, *ACS Nano* **2015**, *9*, 5884.
[21] Y. He, Y. Zhang, X. Li, Z. Lv, X. Wang, Z. Liu, X. Huang, *Energy Storage Mater.* **2018**, *14*, 392.
[22] M. Wang, X. Cheng, T. Cao, J. Niu, R. Wu, X. Liu, Y. Zhang, *J. Alloys Compd.* **2021**, *865*, 158748.
[23] Y. Sun, M. Amirmaleki, Y. Zhao, C. Zhao, J. Liang, C. Wang, K. R. Adair, J. Li, T. Cui, G. Wang, R. Li, T. Filleter, M. Cai, T.-K. Sham, X. Sun, *Adv. Energy Mater.* **2020**, *10*, 2001139.
[24] Y. Sun, Y. Zhao, J. Wang, J. Liang, C. Wang, Q. Sun, X. Lin, K. R. Adair, J. Luo, D. Wang, R. Li, M. Cai, T.-K. Sham, X. Sun, *Adv. Mater.* **2019**, *31*, 1806541.
[25] Y. Zhao, L. V. Goncharova, Q. Sun, X. Li, A. Lushington, B. Wang, R. Li, F. Dai, M. Cai, X. Sun, *Small Methods* **2018**, *2*, 1700417.
[26] F. Mattelaer, P. M. Vereecken, J. Dendooven, C. Detavernier, *Adv. Mater. Interfaces* **2017**, *4*, 1601237.
[27] S. E. Atanasov, B. Kalanyan, G. N. Parsons, *J. Vacuum Sci. Technol. A* **2016**, *34*, 01A148.
[28] S.-K. Otto, Y. Moryson, T. Krauskopf, K. Peppler, J. Sann, J. Janek, A. Henss, *Chem. Mater.* **2021**, *33*, 859.
[29] X. Wei, Z. Meng, L. Ruiz, W. Xia, C. Lee, J. W. Kysar, J. C. Hone, S. Keten, H. D. Espinosa, *ACS Nano* **2016**, *10*, 1820.
[30] G.-H. Lee, R. C. Cooper, S. J. An, S. Lee, A. van der Zande, N. Petrone, A. G. Hammerberg, C. Lee, B. Crawford, W. Oliver, J. W. Kysar, J. Hone, *Science* **2013**, *340*, 1073.
[31] Y. Zhang, G. Wang, L. Tang, J. Wu, B. Guo, M. Zhu, C. Wu, S. X. Dou, M. Wu, *J. Mater. Chem. A* **2019**, *7*, 25369.
[32] L. Chen, Z. Huang, R. S. Yassar, J. A. Libera, K. C. Klavetter, K. R. Zavadil, J. W. Elam, *ACS Appl. Mater. Interfaces* **2018**, *10*, 7043.
[33] P. Biswal, S. Stalin, A. Kludze, S. Choudhury, L A. Archer, *Nano Lett.* **2019**, *19*, 8191.
[34] K R. Adair, C. Zhao, M. N. Banis, Y. Zhao, R. Li, M. Cai, X. Sun, *Angew. Chem.* **2019**, *131*, 15944.
[35] Q. Zhao, Z. Tu, S. Wei, K. Zhang, S. Choudhury, X. Liu, L A. Archer, *Angew. Chem.* **2018**, *130*, 1004.
[36] F. Shi, A. Pei, A. Vailionis, J. Xie, B. Liu, J. Zhao, Y. Gong, Yi Cui, *Proc. Nat. Acad. Sci.* **2017**, *114*, 12138.
[37] Y. Zhao, M. Amirmaleki, Q. Sun, C. Zhao, A. Codirenzi, L V. Goncharova, C. Wang, K. Adair, X. Li, X. Yang, F. Zhao, R. Li, T. Filleter, M. Cai, X. Sun, *Matter* **2019**, *1*, 1215.